# Regrowth-free high-gain InGaAsP/InP active-passive platform via ion implantation

**John S. Parker,[1,*] Abirami Sivananthan,[1] Erik Norberg,[2] and Larry A. Coldren[1]**

[1]*Electrical and Computer Engineering Department, University of California at Santa Barbara, Santa Barbara, CA 93106, USA*

[2]*Aurrion Inc., 130 Robin Hill Road #300, Goleta, CA 93117, USA*

[*] *jparker@ece.ucsb.edu*

**Abstract:** We demonstrate a regrowth-free material platform to create monolithic InGaAsP/InP photonic integrated circuits (PICs) with high-gain active and low-loss passive sections via a PL detuning of >135 nm. We show 2.5 µm wide by 400 µm long semiconductor optical amplifiers with >40 dB/mm gain at 1570 nm, and passive waveguide losses <2.3 dB/mm. The bandgap in the passive section is detuned using low-energy 190 keV channelized phosphorous implantation and subsequent rapid thermal annealing to achieve impurity-induced quantum well intermixing (QWI). The PL wavelengths in the active and passive sections are 1553 and 1417 nm, respectively. Lasing wavelengths for 500 µm Fabry-Perot lasers are 1567 and 1453 nm, respectively.

©2012 Optical Society of America

**OCIS codes:** (250.3140) Integrated optoelectronic circuits; (140.4480) Optical amplifiers; (140.5960) Semiconductor lasers.

## References and links

1. Y. Cheng, J. Pan, S. Liang, W. Feng, Z. Liao, F. Zhou, B. Wang, L. Zhao, H. Zhu, and W. Wang, "Butt-coupled MOVPE growth for high-performance electro-absorption modulator integrated with a DFB laser," J. Cryst. Growth **308**(2), 297–301 (2007).
2. M. Aoki, M. Suzuki, H. Sano, T. Kawano, T. Ido, T. Taniwatari, K. Uomi, and A. Takai, "InGaAs/InGaAsP MQW electroabsorption modulator integrated with a DFB laser fabricated by band-gap energy control selective-area MOCVD," J. Quantum Electron. **29**(6), 2088–2096 (1993).
3. T. K. Ong, Y. C. Chan, Y. L. Lam, and B. S. Ooi, "Wavelength tuning in InGaAs/InGaAsP quantum well lasers using pulsed-photoabsorption-induced disordering," Appl. Phys. Lett. **78**(18), 2637–2639 (2001).
4. T. K. Ong, O. Gunawan, B. S. Ooi, Y. L. Lam, Y. C. Chan, Y. Zhou, A. S. Helmy, and J. H. Marsh, "High-spatial-resolution quantum-well intermixing process in GaInAs/GaInAsP laser structure using pulsed-photoabsorption-induced disordering," J. Appl. Phys. **87**(6), 2775–2779 (2000).
5. B. C. Qiu, A. C. Bryce, R. M. de la Rue, and J. H. Marsh, "Monolithic integration in InGaAs-InGaAsP multiquantum-well structure using laser processing," IEEE Photon. Technol. Lett. **10**(6), 769–771 (1998).
6. H. S. Djie, T. Mei, J. Arokiaraj, C. Sookdhis, S. F. Yu, L. K. Ang, and X. H. Tang, "Experimental and theoretical analysis of argon plasma-enhanced quantum-well intermixing," J. Quantum Electron. **40**(2), 166–174 (2004).
7. H. S. Djie, C. Sookdhis, T. Mei, and J. Arokiaraj, "Photonic integration using inductively coupled argon plasma enhanced quantum well intermixing," Electron. Lett. **38**(25), 1672–1673 (2002).
8. K.-H. Lee, J. O'Callaghan, B. Roycroft, C. L. Daunt, H. Yang, J. H. Song, F. H. Peters, and B. Corbett, "Quantum well intermixing in AlInGaAs MQW structures through impurity-free vacancy method," Proc. SPIE **7604**, 76040J, 76040J-7 (2010).
9. S. K. Si, D. H. Yeo, H. H. Yoon, and S. J. Kim, "Area selectivity of InGaAsP-InP multiquantum-well intermixing by impurity-free vacancy diffusion," IEEE J. Sel. Top. Quantum Electron. **4**(4), 619–623 (1998).
10. J. Zhao, Z. C. Feng, Y. C. Wang, J. C. Deng, and G. Xu, "Luminescent characteristics of InGaAsP/InP multiple quantum well structures by impurity-free vacancy disordering," Surf. Coat. Tech. **200**(10), 3245–3249 (2006).
11. S. Charbonneau, E. S. Koteles, P. J. Poole, J. J. He, G. C. Aers, J. Haysom, M. Buchanan, Y. Feng, A. Delage, F. Yang, M. Davies, R. D. Goldberg, P. G. Piva, and I. V. Mitchell, "Photonic integrated circuits fabricated using ion implantation," IEEE J. Sel. Top. Quantum Electron. **4**(4), 772–793 (1998).
12. P. J. Poole, S. Charbonneau, G. C. Aers, T. E. Jackman, M. Buchanan, M. Dion, R. D. Goldberg, and I. V. Mitchell, "Defect diffusion in ion implanted AlGaAs and InP: Consequences for quantum well intermixing," J. Appl. Phys. **78**(4), 2367–2371 (1995).
13. M. Pantouvaki, C. C. Renaud, P. Cannard, M. J. Robertson, R. Gwilliam, and A. J. Seeds, "Fast tuneable InGaAsP DBR laser using quantum-confined stark-effect-induced refractive index change," IEEE J. Sel. Top. Quantum Electron. **13**(5), 1112–1121 (2007).

#170927 - $15.00 USD Received 26 Jun 2012; revised 1 Aug 2012; accepted 1 Aug 2012; published 15 Aug 2012

14. M. Paquette, V. Aimez, J. Beauvais, J. Beerens, P. J. Poole, S. Charbonneau, and A. P. Roth, "Blueshifting of InGaAsP-InP laser diodes using a low-energy ion-implantation technique: comparison between strained and lattice-matched quantum-well structures," IEEE J. Sel. Top. Quantum Electron. **4**(4), 741–745 (1998).
15. V. Aimez, J. Beauvais, J. Beerens, D. Morris, H. S. Lim, and B. S. Ooi, "Low-energy ion-implantation-induced quantum-well intermixing," IEEE J. Sel. Top. Quantum Electron. **8**(4), 870–879 (2002).
16. M. Chicoine, A. Francois, C. Tavares, S. Chevobbe, F. Schiettekatte, V. Aimez, J. Beauvais, and J. Beerens, "Effects of damage accumulation on quantum well intermixing by low-energy ion implantation in photonic devices," Proc. SPIE **5260**, 423–431 (2003).
17. D. Barba, B. Salem, D. Morris, V. Aimez, J. Beauvais, M. Chicoine, and F. Schiettekatte, "Ion channeling effects on quantum well intermixing in phosphorus-implanted InGaAsP/InGaAs/InP," J. Appl. Phys. **98**(5), 054904–054908 (2005).
18. E. J. Skogen, J. W. Raring, J. S. Barton, S. P. DenBaars, and L. A. Coldren, "Postgrowth control of the quantum-well band edge for the monolithic integration of widely tunable lasers and electroabsorption modulators," IEEE J. Sel. Top. Quantum Electron. **9**(5), 1183–1190 (2003).
19. J. W. Raring and L. A. Coldren, "40-Gb/s Widely Tunable Transceivers," IEEE J. Sel. Top. Quantum Electron. **13**(1), 3–14 (2007).
20. W. Guo, Q. Lu, M. Nawrocka, A. Abdullaev, J. O'Callaghan, M. Lynch, V. Weldon, and J. F. Donegan, "Integrable Slotted Single-Mode Lasers," IEEE Photon. Technol. Lett. **24**(8), 634–636 (2012).
21. M. Silver and E. P. O'Reilly, "Optimization of long wavelength InGaAsP strained quantum-well lasers," J. Quantum Electron. **31**(7), 1193–1200 (1995).
22. T. Takeda, S. Tazawa, and A. Yoshii, "Precise ion-implantation analysis including channeling effects," IEEE Trans. Electron Devices **33**(9), 1278–1285 (1986).
23. J. Bausells, G. Badenes, and E. Lora-Tamayo, "Calculation of channeling effects in ion implantation," Nucl. Instrum. Meth. B **55**(1-4), 666–670 (1991).
24. Y.-F. Lao, H. Wu, and Z.-C. Huang, "Luminescent properties of annealed and directly wafer-bonded InAsP/InGaAsP multiple quantum wells," Semicond. Sci. Technol. **20**(6), 615–620 (2005).
25. C. Blaauw, B. Emmerstorfer, D. Kreller, L. Hobbs, and A. J. Springthorpe, "Effects of S, Si, or Fe dopants on the diffusion of Zn in InP during MOCVD," J. Electron. Mater. **21**(2), 173–179 (1992).
26. E. F. Schubert, C. J. Pinzone, and M. Geva, "Phenomenology of Zn diffusion and incorporation in InP grown by organometallic vapor-phase epitaxy (OMVPE)," Appl. Phys. Lett. **67**(5), 700–702 (1995).
27. N. Yoshimoto, Y. Shibata, S. Oku, S. Kondo, and Y. Noguchi, "Design and demonstration of polarization insensitive Mach-Zehnder switch using a lattice-matched ingaalas/inalas mqw and deep-etched high-mesa waveguide structure," J. Lightwave Technol. **17**(9), 1662–1668 (1999).

## 1. Introduction

The InGaAsP/InP heterostructure is one of the most widely used material systems for 1.55 μm telecommunication lasers and photonic integrated circuits (PICs). Numerous methods have been investigated to create an InGaAsP/InP monolithically integrated platform with both active (material with optical gain) and passive (material with low propagation loss) sections. These include butt-joint regrowth [1], selective area regrowth (SAG) [2], and quantum-well disordering [3–19], often referred to as quantum-well intermixing (QWI), in which the quantum well and barrier compositions are interdiffused.

Only QWI can shift the bandgap post-growth, and can thus alleviate complexities arising from regrowth and provide cost savings by avoiding additional growths. Regrowth contamination is unavoidable in most facilities, especially from silicon, which as an N-type InP dopant can be detrimental to correct placement of the p-i-n junction, and hence for efficient carrier injection into the QWs. QWI provides the lowest refractive index discontinuity between active-passive sections as the overall material composition in the waveguide remains the same, while the composition in the QWs and barriers is shifted. This is highly beneficial as reflections caused by refractive index discontinuities make on-chip lasers unstable through unwanted optical feedback.

Many techniques have demonstrated QWI, with varying trade-offs. These include photo-absorption induced disordering (PAID) [3–5], inductively coupled plasma quantum well intermixing (ICP-QWI) [6, 7], impurity-free vacancy disordering (IFVD) [8–10], and impurity-induced disordering (IID) [11–19]. In all methods, defects are diffused through the material with a rapid thermal anneal (RTA) above 600 °C, and the extent of the disordering is measured by the change in the wavelength of the photoluminescence peak (PL).

IID relies on ion implantation of a benign atom, e.g. phosphorous or arsenic, to create vacancies near the QWs. To reduce the implant energy yet still achieve large >100 nm blue shifts, many researchers have implanted without the p-type cladding grown, and then regrow

#170927 - $15.00 USD Received 26 Jun 2012; revised 1 Aug 2012; accepted 1 Aug 2012; published 15 Aug 2012
(C) 2012 OSA

to finish the device [18, 19]. For gratings definition on the waveguide, this regrowth is necessary, however avoiding this regrowth can reduce fabrication time, improve yield, and reduce risks inherent in regrowth near the p-i-n junction. Towards this aim, recent work has demonstrated that higher-order gratings can be successfully fabricated from the top of the laser structure, providing excellent side-mode-suppression (>50 dB), without the need for regrowth [20].

Early regrowth-free experiments demonstrated maximum shifts of 90 nm for 3 MeV $P^+$ ions implanted into an InP laser structure at 7° tilt, whereas 200 keV implants produced <35 nm shifts [12]. The QWs were located 1.85 µm below the upper InP surface, and >1.5 MeV energy was necessary to create any defects near the QWs. However, there are several drawbacks to MeV implants including: a thick dielectric or metal implant mask is necessary to block the implant for nonintermixed regions (e.g. 3 MeV $P^+$ simulated with the Stopping Range of Ions in Solids software (SRIM) shows the necessary $SiO_2$ mask thickness to be >2.75 µm), and the majority of ion implantation vendors only provide single-ionized energies <200 keV. Reduction of ion energy below 200 keV allows for ease of manufacturing, yet angled implants at keV energies can only provide limited bandgap shifts for full laser structures. For example, a 37 nm PL blue shift was demonstrated for the phase and grating sections of a DBR using 100 keV $P^+$ at 7° tilt [13]. Some researcher have overcome the ion energy limitation by using doubly charged ions for which a 100 nm blue shift was demonstrated using 360 keV $P^{++}$ at 7° tilt [14, 15].

To avoid regrowth with <200 keV implant energy, one solution is to implant deeper using ion channeling. Compared to angled implantation, ion channeling has an increased implantation depth, results in a greater PL shift in the QWs, and has a lower density of nonradiative recombination centers after RTA [17]. Yet, ion channeling is avoided in silicon CMOS and bipolar technology. Angled (i.e. nonchannelized) implantation produces a near gaussian implant profile at the desired depth, whereas channeling creates a broad implant profile that varies with implant angle. For Si CMOS, precise junction placement is achieved via implantation and any angular spread over the sample results in an implant depth variation. However, for PIC applications requiring only two waveguide bandgaps, a high-gain active and a low-loss passive, the implant depth tolerances are much greater than in CMOS. For example, a passive section may simply need to be low-loss with a PL detuned by ~110 nm from the active section. An extreme variation in detuning of as much as 20% ( ± 11 nm) across a wafer due to implant and RTA results in a passive loss variation of only ~1 $cm^{-1}$ [18]; this is less than 0.5 dB loss for extremely large 1 mm long passive components. In this case, a material platform with 20% detuning variation in the intermixed regions can be acceptable for many PIC components including: semiconductor optical amplifiers, QW detectors, star couplers and arrayed waveguide gratings, multimode interference couplers, and passive waveguides.

In this paper, we demonstrate that ion channeling, i.e. 0° tilt, can provide this much needed reduction in implant energy for regrowth-free fabrication of lasers with active and passive sections. A blue shift of >135 nm is achieved using a 190 keV phosphorous implant with a subsequent 670 °C RTA for 120 s. This is the largest blue shift yet demonstrated for regrowth-free IID, and greater than the PL shift shown using 7° tilt 3 MeV $P^+$ [12], meanwhile the implant energy used is 15X lower and the anneal temperature is 30 °C below that used in [12]. Previous studies demonstrate the benefits of ion-channeling on intermixing InGaAsP QWs; however, only a 42 nm blue shift is shown and the structure used requires a cladding and contact regrowth [17]. One of the main concerns for regrowth-free processing is diffusion of the p-type Zn dopant during the RTA. To examine the effects of Zn diffusion, we present Secondary Ion Mass spectroscopy (SIMs), passive loss, and active gain measurements from devices fabricated with this method. A thick layer structure is used in the experiment to examine the feasibility of the process at the upper limits of p-cladding designs, where the QWs are placed 2.45 µm from the surface, as shown in Fig. 1(a). The majority of laser structures will have thinner cladding layers and can use lower implant energy to achieve this detuning.

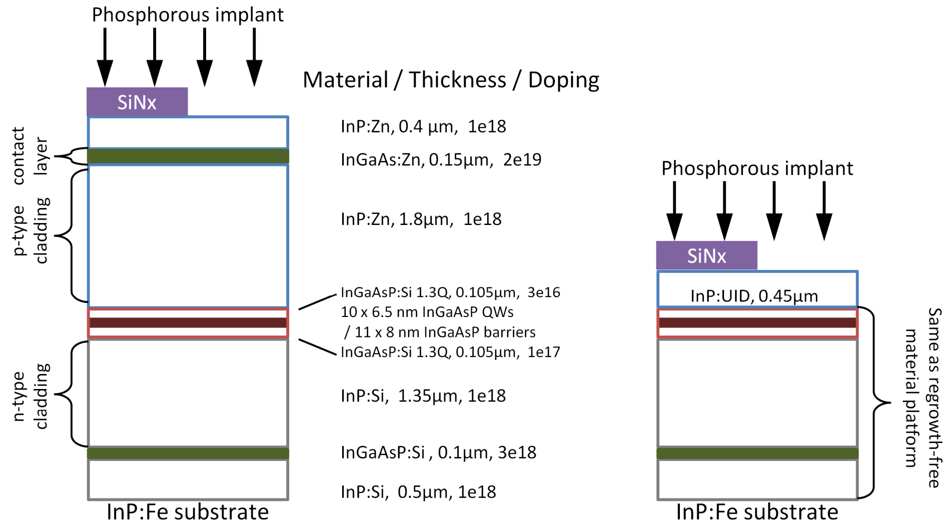


Fig. 1. Cross-sections of the two material platforms investigated for impurity-induced disordering. SiNx acts as a mask to prevent phosphorous implantation into the active regions. (a) The regrowth-free material platform that requires no additional growth steps to fabricate active-passive laser structures. Ions are implanted into the passive (nonmasked) regions and channel through the InP lattice to reach the QWs. (b) The material platform that requires additional regrowth steps for the p-type cladding and contact layers.

It is important to note that in much of the previously mentioned work [3–7, 11, 12, 14–17], 5.5-6.0 nm $In_{0.53}Ga_{0.47}As$ QWs with 10-20 nm $In_{0.74}Ga_{0.26}As_{0.55}P_{0.45}$ barriers ($\lambda_g = 1.26$) are used to create narrow wells with a high compositional different between QW and barrier, enhancing the effect of disorder on the bandgap. High composition variation and narrow QWs can provide a larger bandgap detuning, yet they do limit the flexibility and performance compared to the InGaAsP/InGaAsP (QW / barrier) material platform [21]. In this study, 6.5 nm (0.9% compressively strained) $In_{0.735}Ga_{0.265}As_{0.845}P_{0.155}$ QWs and 8 nm $In_{0.735}Ga_{0.265}As_{0.513}P_{0.487}$ barriers are used.

## 2. Methodology

The critical angle for high-energy ion implantation can be approximated by [22]:

$$\Phi_c = \sqrt{\frac{Z_1 Z_2 q^2}{2\pi\varepsilon_o E d}}. \tag{1}$$

where $Z_1$ and $Z_2$ are the atomic numbers of the implant species and the target, respectively. E is the energy of the implant, $\varepsilon_o$ is the permittivity of free space, and d is the atomic separation or lattice constant. From this equation, the critical angle is proportional to the square root of the atomic number. For compounds such as InP, a geometric average of the two species is typically used for $Z_2$. For InP, we use $Z \approx \sqrt{Z_{In} Z_P} = 27$, which leads to a 38% larger critical angle for implantation than for Si. The approximation in Eq. (1) requires an additional correction factor for lower energy implants [23], such as 190 keV:

$$\Phi_c^{'} = \sqrt{\frac{\Phi_c \sqrt{1.5a}}{d}}. \tag{2}$$

#170927 - $15.00 USD Received 26 Jun 2012; revised 1 Aug 2012; accepted 1 Aug 2012; published 15 Aug 2012
(C) 2012 OSA

where a is the Thomas-Fermi screening radius for $P^+$ in InP, 0.11-0.12 Å. We find that the critical angle for ion channeling $P^+$ into InP at 190 keV is ~3°. Hence, there is a ± 3° margin for error on the implant while still achieving channeling for the majority of ions.

## 3. Results and discussion

The QW structures are grown on semi-insulating (100) InP iron-doped 2" wafers by metalorganic chemical vapor deposition (MOCVD) at 600-650 °C. A 2.5 cm x 2.5 cm sample is patterned with 600 nm of plasma enhanced chemical vapor deposition (PECVD) SiNx and sent for phosphorous implant at 190 keV, 2e15 ions/cm$^2$ dose with a 200 °C stage temperature, and a 0° ± 1° tilt angle. The SiNx is twice as thick as the implant depth predicted by SRIM simulation, to assure that the active regions are fully protected by the mask and that no vacancies are created in the active region. After implant, the SiNx is removed using BHF and surface defects are removed with a 1 min $O_2$ descum in a Gasonics remote ashing chamber at 250 °C. Afterward, the sample is dipped in 8% (by volume) phosphoric acid for 2 min and rinsed in deionized water, to remove native oxide formed by the ash, and solvent cleaned to remove acid residue. 40 nm of PECVD SiNx is deposited each side of the sample, and a subsequent 2 min 670 ± 3 °C RTA in $N_2$ is used to diffuse the vacancies. Afterward, the SiNx is removed using BHF, and standard photolithography and wet-etches are used to define 2.5 µm wide surface ridge lasers with top N-side Ni/AuGe/Ni/Au and P-side Pt/Ti/Pt/Au contacts. The InGaAs is removed between the P-side contacts for electrical isolation, the substrate is thinned to 120 µm for cleaving, and the sample is tested on a thermo-electric cooled copper stage.

The PL of the passive section near the wafer's center is measured at 1417 nm with an adjacent active PL at 1553 nm, as shown in Fig. 2. The full-width-at-half-maximum (FWHM) and each corresponding PL peak wavelength are listed in Table 1. For these measurements, the pump laser wavelength is 980 nm with 0.75-1.00 W/mm$^2$ power at the wafer surface. The higher powers are necessary for clear PL in the passive areas as the PL intensity decreases from the as-grown PL. The higher pump powers in this range account for a 5% increase in FWHM, when tested on the same sample, therefore slight deviations in the FWHM are due to the range of pump powers. There is variation in the passive PL of ± 10 nm over the processed sample area (a 14% variation in total blue shift), whereas the active variation is ± 2 nm, which matches the as-grown wafer. The larger variation in passive PL results from nonuniformity in the ion implantation and the RTA. The RTA has a ~5 °C temperature gradient across the sample with the thermo-couple placed at the center. The largest PL shift occurs at the hotter side of the wafer, indicating that temperature variation in the RTA is more significant than implant variation for samples of this size. The total PL shift from the as-grown sample is 139 nm, with a detuning between the active and passive regions of 136 nm.

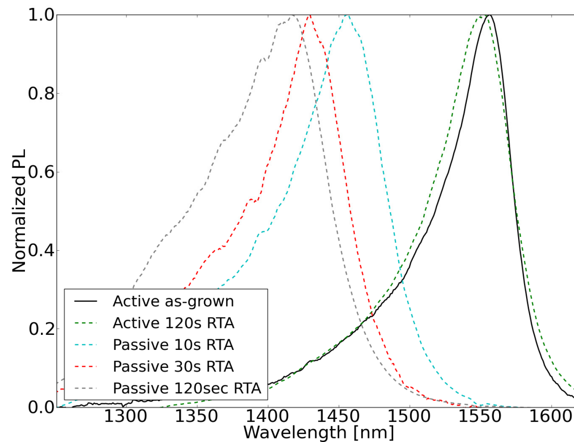


Fig. 2. (Regrowth-free sample) PL shift due to impurity-induced disordering during rapid thermal anneal (RTA) at 670 °C for InGaAsP/InGaAsP QWs and barriers with 1.8 μm InP:Zn cladding, 0.1 μm InGaAs:Zn contact, and 0.4 μm InP:Zn cap layers.

**Table 1. PL during 670 °C RTA on regrowth-free sample**

| | As-grown | Active 120s | Passive 10s | Passive 30s | Passive 120s |
|---|---|---|---|---|---|
| PL [nm] | 1556 | 1553 | 1455 | 1429 | 1417 |
| FWHM [nm] | 57 | 64 | 80 | 75 | 103 |

For comparison to a regrown QWI sample, intermixing is conducted using the well established method described in [18, 19] using a 450 nm InP:UID implant buffer above the QWs, as shown in Fig. 1 (b). The sample is angled at 7° tilt and $P^+$ implanted at 100 keV, 5e14 ions/cm$^2$ dose with a 200 °C stage temperature. This structure has no Zn doped regions, and provides insight into the channelized defect location and the effect of the Zn doping during intermixing. The PL shift is shown in Fig. 3, with the FWHM and PL peak wavelengths listed in Table 2. The InP:UID clad PL shift is 134 nm with a detuning of 120 nm between the active and passive regions, post-RTA. This sample has the layer structure proposed in [18] and designed for post-QWI InP buffer removal and regrowth. The as-grown PL shift of 14 nm during QWI is common for this platform, due to diffusion of surface defects into the QWs, as used in IFVD for bandgap detuning. The regrowth-free layer structure, shown in Table 1, has only a 3 nm shift during QWI as diffusion of surface defects does not reach the QWs with this thicker structure.

Determining the phosphorous depth after implant is challenging as SIMs cannot differential the implanted $P^+$ ions from the phosphorous in InP material structure. Rutherford backscattering spectrometry (RBS) can be used to investigate defect distributions within crystals, but high RBS sensitivity is required to analyze implant induced defects at 200 °C due to in situ diffusion, and low defect concentration often cannot be resolved [16]. Channelized implants are complicated to simulate, and accurate models in use for channeling in Si require large experimental data sets for interpolation. However, angled implants can be simulated with higher accuracy. For the 7° tilt 100 keV $P^+$ implant, SRIM predicts a 110 nm mean depth, 53 nm straggle, and a maximum depth of 250 nm. Therefore, in Fig. 3 the implanted ions are >300 nm from the QWs. As shown in Table 1 and 2, the channelized ion implant 2.45 μm above the QWs shifts the PL faster than the angled implant 550 nm above the QWs. After a 30 s RTA, 1429 nm and 1493 nm PLs are observed for the channelized and angled ion implant, respectively. The rates of PL detuning suggests that channelized defects are at an equal or closer distance from the QWs after implant, that is <300 nm. However, doping (Zn vs. UID), defect concentration, defect distribution, and the type of defects formed do influence the diffusion of vacancies for QWI.

#170927 - $15.00 USD Received 26 Jun 2012; revised 1 Aug 2012; accepted 1 Aug 2012; published 15 Aug 2012
(C) 2012 OSA

Comparing the InP:Zn cladding to the UID cladding, there is a dramatic increase in the FWHM for the InP:Zn intermixed passive sections. The InP:UID sample has no Zn in the structure, and therefore has no Zn diffusion into the QWs during the RTA process. There are two mechanisms for the Zn doping to cause PL broadening. In the first, Zn enhances the monolayer variations in the QW thicknesses. Minor spatial variation in QW thickness is frequently observed during RTA and quantum well disordering [24]. In the second, Zn incorporation in the QWs causes intraband carrier scattering, and leads to homogenous broadening.

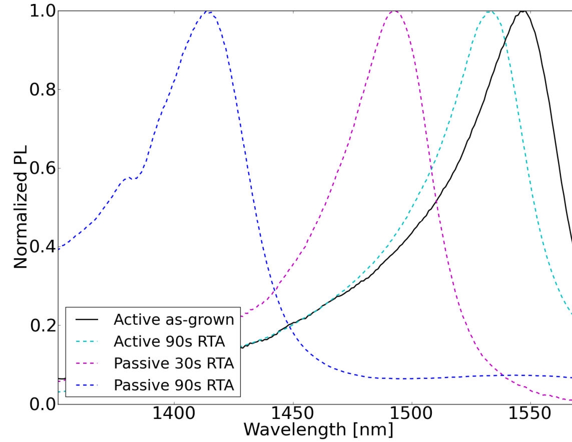


Fig. 3. (Sample requiring regrowth) PL shift due to impurity-induced disordering during rapid thermal anneal (RTA) at 670 °C for InGaAsP/InGaAsP QWs and barriers with 450 nm InP:UID buffer layer, see layer structure in Fig. 1(b).

**Table 2. PL during 670 °C RTA on sample requiring regrowth**

| | Active-as-grown | Active 90s | Passive 30s | Passive 90s |
|---|---|---|---|---|
| Peak PL [nm] | 1548 | 1534 | 1493 | 1414 |
| FWHM [nm] | 56 | 52 | 48 | 63 |

The Zn doping profiles of the regrowth-free as-grown and passive (after implant and RTA) are examined using Secondary Ion Mass spectroscopy and shown in Fig. 4. The Zn doping in the InGaAs contact layer has been reduced from 1.5e19 $cm^{-3}$ to 1e19 $cm^{-3}$, and Zn doping has diffused into the separate confinement heterostructure (SCH) and QWs. The Zn doping level in the QWs is ~1.5e17 $cm^{-3}$, with Zn doping in the SCH from 1e17 $cm^{-3}$ to 2.5e17 $cm^{-3}$. The Zn doping decreases abruptly to 8e16 $cm^{-3}$ at the InP-SCH interface; the reason for this dip is unknown yet it has been observed on the SIMS characterization for two additional QWI samples. The Si doping inhibits the Zn diffusion for concentration of Zn below Si, which likely explains why the tail of the Zn diffusion does not extend into the lower cladding with 1e18 $cm^{-3}$ Si, whereas the SCH with 3e16-1e17 $cm^{-3}$ Si has a minimal effect [25]. The Zn diffusion is much greater for the implanted samples due to defect assisted diffusion. Without added vacancies present, typical Zn at 1e18 $cm^{-3}$ concentration in InP diffuses <22 nm at 700 °C for 120 s, using the diffusion constants measured in [26].

#170927 - $15.00 USD Received 26 Jun 2012; revised 1 Aug 2012; accepted 1 Aug 2012; published 15 Aug 2012
(C) 2012 OSA

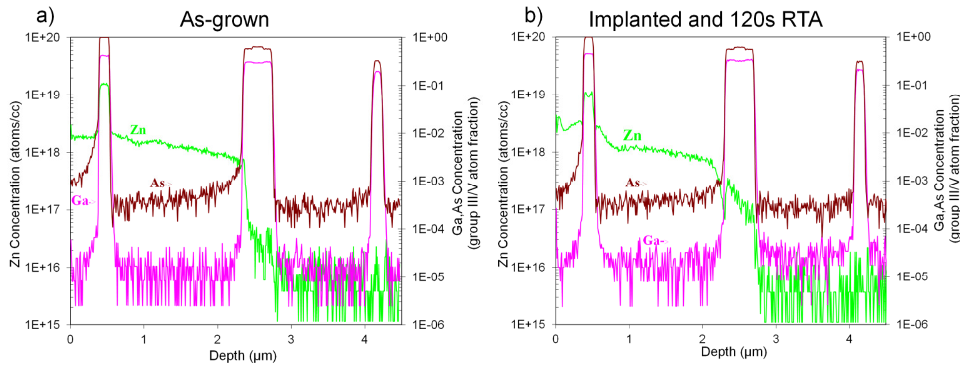


Fig. 4. Secondary Mass Ions spectroscopy of (a) the as-grown regrowth-free InGaAsP/InP material, and (b) passive areas of the regrowth-free material after 190 keV $P^+$ implant and subsequent 120 s anneal at 670 °C. The material structure is shown in Fig. 1(a).

The losses of the passive waveguides are characterized by measuring the transmission $|S_{21}|^2$ of cleaved Fabry-Perot (FP) cavities, as shown in Fig. 5. The TE polarization of an ASE source is selected with a polarization beam splitter (PBS) and launched into the waveguide using a lensed fiber. The FP response is captured with a second lens fiber and measured on an optical spectrum analyzer (OSA) with 0.06 nm resolution. The $|S_{21}|^2$ response from one of these test structures is shown in Fig. 6. The average TE mode passive loss from a set of 5 adjacent FP structures with length 1775 µm is 5.5 ± 1 cm$^{-1}$, i.e. 2.3 dB/mm; the uncertainty arises from fiber drift affecting the fit of $|S_{21}|^2$. These passive losses are confirmed by measuring the change in differential quantum efficiency for active-passive (500 µm-700 µm) lasers during cleave-back, with an extracted passive loss of 6 ± 2 cm$^{-1}$. The free carrier absorption loss resulting from Zn and Si doping in InP has been reported on in literature [27]. With these numbers, a modal free carrier absorption loss 4 cm$^{-1}$ is estimated from Rsoft BeamProp simulation using the layers and doping concentrations measured by SIMS, see Fig. 4(b).

By preventing Zn diffusion into the SCH and reducing the Zn doping to 5e17 cm$^{-3}$ in the lower half of the p-type cladding, the estimated free carrier absorption losses can be reduced to ~2 cm$^{-1}$. Therefore, passive propagation losses would benefit greatly from an optimized doping set-back or super-lattice, to inhibit the p-type doping from entering the SCH layer after the intermixing process. Further investigation is required as super-lattices can be detrimental to intermixing by capturing defects and reducing their diffusion to the QWs. Due to the high doping level in the contact layer, some Zn diffusion out of the InGaAs during RTA is likely, which results in a higher contact resistance in the passive sections. A QWI process followed by regrowth has the potential for less Zn diffusion in the SCH, i.e. lower free-carrier absorption, and additional functionality provided by the multiple growths. A prior study investigated multiple regrowths on a QWI sample with a UID set-back layer, and measured passive loss of 1.8 cm$^{-1}$ [19]. The trade-off with additional growth steps is the added cost and time involved in loading the samples in the reactor, and the risk of contamination (or reduced yield) at the regrowth interface from silicon (as n-type dopant) and other processing contaminants. As growth is increasingly centralized and wafers shipped away for each growth, minimizing the numbers of regrowths is desirable. Certain PIC designs, such as those involving unitraveling carrier (UTC) detectors or varying QW placement in the cladding [19], will always require multiple growths, whereas others can be made regrowth-free.

#170927 - $15.00 USD Received 26 Jun 2012; revised 1 Aug 2012; accepted 1 Aug 2012; published 15 Aug 2012
(C) 2012 OSA

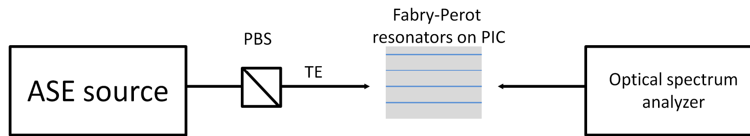


Fig. 5. Test set-up for measurement of TE polarized optical losses of passive Fabry-Perot resonators. Amplified spontaneous emission (ASE). Polarization beam splitter (PBS).

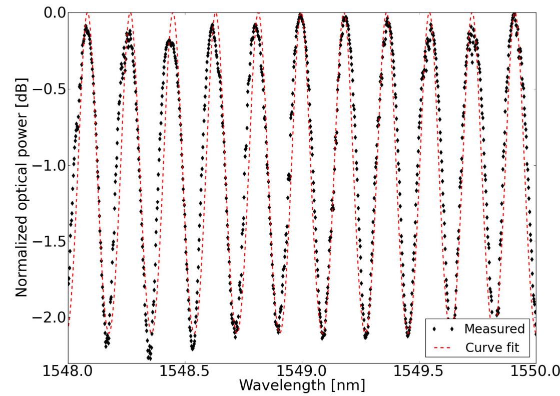


Fig. 6. (Regrowth-free sample) Measured $|S_{21}|^2$ response of 1775 µm long Fabry-Perot resonators with ASE input. Lower losses correspond to higher extinction values in the response. Curve fit is 5.5 $cm^{-1}$ propagation loss.

The active waveguides are characterized by measuring the large signal gain of an optical mode through a semiconductor optical amplifier (SOA). Three 400 µm SOAs are cascaded serially. For the gain test, the first SOA is reversed biased at −1 V to detect the coupled optical power then it is forward biased up to 2 V to provide gain to this optical mode. The second SOA is reverse biased to detect the gain provided by the first SOA. The electrical isolation between the two sections is >5 kΩ, and current leakage is measured and subtracted from total current in order to measure the optical gain. The measurement uncertainty is ± 2 dB/mm due to fiber coupling drift and current leakage. The optical gain peak is at 1570 nm for a set 25 °C stage temperature. A 1 mW tunable laser is fiber coupled into the test structure, and gain of 40 dB/mm is measured at 6.3 $kA/cm^2$, as shown in Fig. 7.

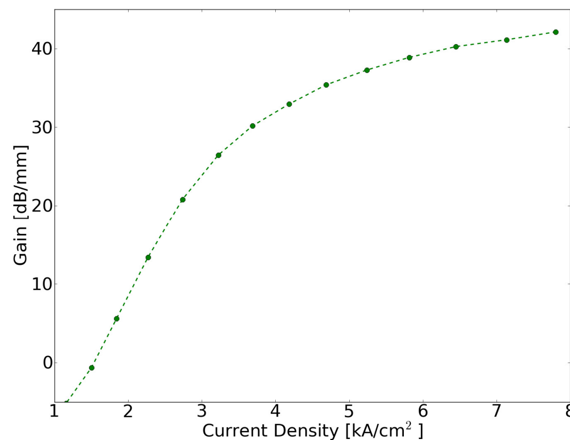


Fig. 7. (Regrowth-free sample) Measured large signal gain vs. current density for a 400 µm active semiconductor optical amplifier at 25 °C. Injection efficiency of 75% assumed.

#170927 - $15.00 USD Received 26 Jun 2012; revised 1 Aug 2012; accepted 1 Aug 2012; published 15 Aug 2012
(C) 2012 OSA

The pulsed lasing of active FP cavities is measured using 1 µs current pulses and a large area InGaAs photodetector. The threshold currents for 500 µm x 2.5 µm lasers at ~1567 nm and 1452 nm are shown in Table 3. The lasing spectra of the two lasers at $1.1xI_{th}$ is shown in Fig. 8. The pulsed threshold current for the intermixed laser is ~2X higher, likely caused by broadening of the gain spectrum and Zn diffusion into the QWs increasing the internal loss through free-carrier absorption.

**Table 3. Fabry-Perot pulsed and cw threshold currents on regrowth-free sample**

| | Lasing at 1567nm* | Lasing at 1452nm* |
|---|---|---|
| $I_{th}$ (mA), $J_{th}$ (kA/cm$^2$) Pulsed | 19, 1.14 | 42, 2.52 |
| $I_{th}$ (mA), $J_{th}$ (kA/cm$^2$) CW | 22, 1.32 | 53, 3.18 |

*lasing wavelength measured under CW operation

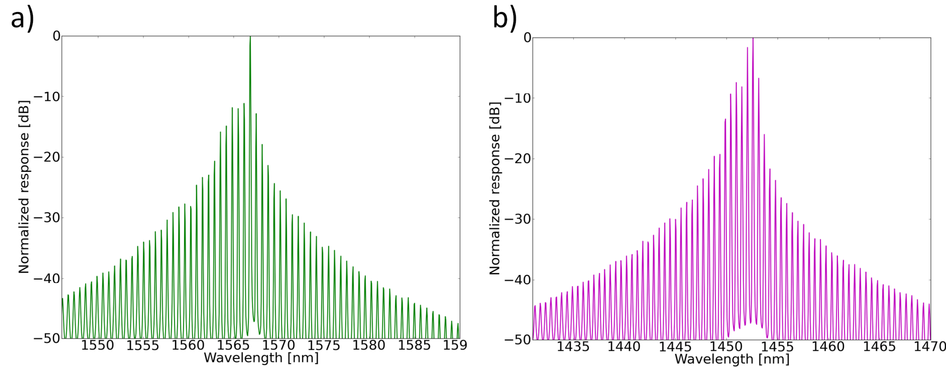


Fig. 8. Regrowth-free sample (a) optical spectra of Fabry-Perot laser made from active material with PL 1553 nm at $1.1I_{th}$, and (b) made from passive material with PL 1417 nm at $1.1I_{th}$.

## 3. Conclusion

We have shown ridge lasers fabricated with a regrowth-free active-passive InGaAsP/InP platform, using a channelized phosphorous ion implantation at 190 keV. The quantum wells are positioned 2.45 µm below the implanted surface, indicating that this process is even suitable for material platforms with thick cladding layers. The active sections have high gain >40 dB/mm, whereas the passive sections have losses <2.3 dB/mm. This process is promising for the creation of large-area regrowth-free PICs, and for rapid optimization of new photonic components where fast processing turnaround time is required. By avoiding regrowth defects and interface contamination, high-yield and high-performance photonic components can be fabricated.

## Acknowledgment

This work was supported by the Defense Advanced Research Projects Agency (DARPA) under the Photonic Integrated for Coherent Optics (PICO) program. A portion of this work was conducted in the UCSB nanofabrication facility, part of the NSF funded NNIN network.

#170927 - $15.00 USD Received 26 Jun 2012; revised 1 Aug 2012; accepted 1 Aug 2012; published 15 Aug 2012
(C) 2012 OSA